Supplementary information: Coherent helicity-dependent spin-phonon oscillations in the ferromagnetic van der Waals crystal CrI$_3$

P. Padmanabhan[1,†,*], F. L. Buessen[2,†], R. Tutchton[1], K. W. C. Kwock[1,3], S. Gilinsky[1], M. C. Lee[1],

M. A. McGuire[4], S. R. Singamaneni[5], D. A. Yarotski[1], A. Paramekanti[2,*], J.-X. Zhu[1,*],

R. P. Prasankumar[1,6,*]

[1]Center for Integrated Nanotechnologies, Los Alamos National Laboratory, Los Alamos, NM 87545, USA

[2]Department of Physics, University of Toronto, Toronto, Ontario M5S 1A7, Canada

[3]The Fu Foundation School of Engineering and Applied Science, Columbia University, New York, NY 10027, USA

[4]Materials Science and Technology Division, Oak Ridge National Laboratory, Oak Ridge, TN 37831, USA

[5]Department of Physics, The University of Texas at El Paso, El Paso, TX 79968, USA

[6]Deep Science Fund, Intellectual Ventures, Bellevue, WA 98005, USA

† Authors contributed equally

* Authors to whom correspondence should be addressed: prashpad@lanl.gov, arunp@physics.utoronto.ca, jxzhu@lanl.gov, rpprasan@lanl.gov

22 *The Mott Density Criterion*

23   To estimate the photoexcited carrier density, we begin by estimating the relevant optical

24 constants of CrI_3. The complex dielectric functions and associated complex refractive index for

25 right circularly polarized (σ_+) and left circularly polarized (σ_-) light can be computed from the

26 linear dielectric response functions as

27
$$\tilde{\epsilon}_\pm = \tilde{\epsilon}_{xx} + i\tilde{\epsilon}_{xy}, \text{ and} \tag{1}$$

28
$$\tilde{n}_\pm = \sqrt{\tilde{\epsilon}_{xx} + i\tilde{\epsilon}_{xy}}. \tag{2}$$

29 This allows us to obtain the normal incidence reflectivity and absorption coefficients as

30
$$R_\pm = \left|\frac{\tilde{n}_\pm - 1}{\tilde{n}_\pm + 1}\right|^2, \text{ and} \tag{3}$$

31
$$\alpha_\pm = \frac{4\pi}{\lambda}\mathfrak{I}\{\tilde{n}_\pm\}. \tag{4}$$

32 Assuming a spin-up domain and using the calculated linear dielectric functions[1], we estimate the

33 σ_+ reflectivity and absorption coefficient at $E_p = 1.55$ eV to be approximately $R_+ = 0.148$ and

34 $\alpha_+ = 1.81 \times 10^4$ cm^{-1}, respectively. In contrast, for σ_- photons, $R_- = 0.135$ and $\alpha_- = 2.87 \times 10^2$

35 cm^{-1}, highlighting the dramatically larger absorption of σ_+ light in spin-up domains. Despite the

36 lack of ellipsometry data for CrI_3 in this energy range below the Curie temperature (T_c), we note

37 that differential reflectivity measurements made on bulk-like flakes[2] yield absorption coefficients

38 that are reasonably close to the calculated values.

39   Using the above parameters, we can estimate the electron-hole pair density that is

40 photoexcited as a function of thickness to be[3]

41
$$N_\pm(z) = \frac{\alpha_\pm(1-R_\pm)F}{E_p}e^{-\alpha_\pm z}, \tag{5}$$

42 where F is the fluence of the ultrafast pump pulse. Given our ~20 μm spot diameter and

43   photoexcitation depth of ~550 nm[1], we calculate a photoexcited carrier density of $N_+ =$

44   2.50×10^{19} cm^{-3} and $N_- = 6.33\times10^{17}$ cm^{-3}. Given the nanometer-scale exciton radius of van der

45   Waals materials, the former density is likely to be large enough to exceed the Mott density

46   criterion of $n_c = (0.25/a_B^*)^3$, yielding a transient photoinduced quasi-metallic state. This

47   supports our interpretation of the demagnetization dynamics under the microscopic three-

48   temperature model, typically applied to the case of ferromagnetic metals.

49

50   *Microscopic Three-Temperature Model*

51   We model the experimentally measured demagnetization dynamics using the microscopic three-

52   temperature model (M3TM), which considers the impact of both conventional electron-phonon

53   scattering and Elliott-Yafet processes that are enabled by spin orbit coupling (SOC). Here, the

54   majority- ($\Uparrow$) and minority-spin ($\Downarrow$) Bloch states ($|\psi\rangle$) are comprised of admixtures of pure spin

55   states $|\uparrow\rangle$ and $|\downarrow\rangle$, such that[4]

$$|\psi_{\mathbf{k}n}^{\Uparrow}\rangle = a_{\mathbf{k}n}^{\uparrow}|\uparrow\rangle + b_{\mathbf{k}n}^{\uparrow}|\downarrow\rangle, \text{ and} \tag{6}$$

$$|\psi_{\mathbf{k}n}^{\Downarrow}\rangle = a_{\mathbf{k}n}^{\downarrow}|\downarrow\rangle + b_{\mathbf{k}n}^{\downarrow}|\uparrow\rangle, \text{ and} \tag{7}$$

58   where $\mathbf{k}$ is the wave vector, n is the band index, and $a_{\mathbf{k}n}^{\uparrow,\downarrow}$ and $b_{\mathbf{k}n}^{\uparrow,\downarrow}$ are the wave function

59   coefficents associated with the pure spin-states. Here, $b_{\mathbf{k}n}^{\uparrow,\downarrow}$ are non-zero only if SOC is present,

60   which allows for a finite probability of phonon-mediated spin-flip scattering with a matrix

61   element of the form[5]

$$g_{mn\mathbf{q}}^{\Downarrow\Uparrow} = \langle \psi_{\mathbf{k}+\mathbf{q}m}^{\Downarrow} | \Delta V_{\mathbf{q}} | \psi_{\mathbf{k}n}^{\Uparrow} \rangle \neq 0 \tag{8}$$

63   where $\mathbf{q}$ is the phonon wave vector and ΔV is the interaction potential.

64   This is the basis of the M3TM, which uses a system of three partial differential equations

65   to describe the interacting electronic, phonon, and spin subsystems as[6]

66
$$C_e(T_e)\frac{dT_e}{dt} = \kappa\nabla_z^2 T_e + G_{ep}[T_p - T_e] - C_e(T_e)\frac{T_e - T_0}{\tau_{\text{th}}} + P_0 G(t), \qquad (9a)$$

67
$$C_p\frac{dT_p}{dt} = G_{ep}[T_e - T_p], \text{ and} \qquad (9b)$$

68
$$\frac{dm}{dt} = Rm\frac{T_p}{T_C}\left[1 - m\coth\left(m\frac{T_C}{T_e}\right)\right], \qquad (9c)$$

69   where T_e is the electronic temperature, T_p is the phonon temperature, and m is the magnetization.

70   The relevant CrI$_3$ material properties are the thermal conductivity κ, the electronic specific heat

71    $C_e = \gamma_e T_e$, where γ_e is the electronic specific heat coefficient, and the phonon specific heat C_p. R

72   is a material-dependent parameter given by[6]

73
$$R = \frac{8a_{\text{sf}}G_{ep}k_B T_c^2 V}{\mu E_D^2}, \qquad (10)$$

74   where k_B is Boltzmann's constant, V is the formula unit volume, μ is the magnetic moment, and

Parameter	Value
κ (Wm^{-1}K^{-1})	1.36
γ (Jm^{-3}K^{-2})	550
C_p (Jm^{-3}K^{-1})	1.5×10^5
V (m^3)	1.35×10^{-28}
μ (μ_B)	3.87
E_D (J)	1.85×10^{-21}
T_c (K)	61

Supplementary Table 1. M3TM material parameters.

Material parameters used in the M3TM that were obtained

from literature. κ was obtained from Ref. 7, γ_e, C_p, μ, E_D,

and T_c were obtained from Ref. 8, and V was estimated

from the material parameters in Ref. [9].

75

76 E_D is the Debye energy. G_{ep}, a_{sf}, τ_{th}, and P_0 are the electron-phonon coupling constant, the spin-

77 flip probability, the thermal diffusion time, and the energy absorption from the Gaussian pump

78 pulse $G(t)$, which are treated as free parameters in the fitting procedure. The material parameters

79 obtained from the literature are summarized in Supplementary Table 1. In particular, the thermal

80 conductivity was obtained directly from DFT calculations presented in Ref. 7. The electronic

81 specific heat coefficient and phonon specific heat were estimated from the low temperature heat

82 capacity, plotted as C/T vs T^2 in Fig. 6c of Ref. 8. This was converted to units of $\text{Jm}^{-3}\text{K}^{-3}$ by

83 multiplying by a conversion factor of $a = 75/2.025 = 37$ by comparison with Refs. [10] and [11]. The

84 intercept of Fig. 6c of Ref. 8 then gives the electronic specific heat coefficient, which can be

85 converted to $\text{J/m}^3\text{K}^2$ by multiplying by the molar mass (432.7 g/mol) and the density

86 $(5.32 \times 10^6 \text{ kg/m}^3)$, which were obtained from Ref. [9]. The phonon specific heat was estimated in

87 the same way from the slope of Fig. 6c of Ref. 8. The formula unit volume was approximated

88 by dividing the molar mass by the density and Avogadro's number. The Debye energy was

89 obtained by multiplying the Debye temperature of 134 K from Ref. 8 by Boltzmann's constant.

90 Finally, the magnetic moment and critical temperature were obtained directly from Ref 8.

91 We solved the system of equations (9) over a temporal window of 400 ps and a depth into the

92 sample of 100 nm. The fit parameters were globally optimized using an algorithm that used

93 multiple initial start points across the parameter space and a constrained minimization process

94 using an interior point algorithm as implemented in MATLAB[12] and a cost function consisting of

95 the absolute difference between the calculated and experimentally obtained magnetization

96 dynamics. This was parallelized using MATLAB's parallel computing toolbox to reduce the

97 computation time. The partial differential equation system outlined in eq. (9) was solved using

98 MATLAB's parabolic-elliptic partial differential equation solver which uses a variable-step,
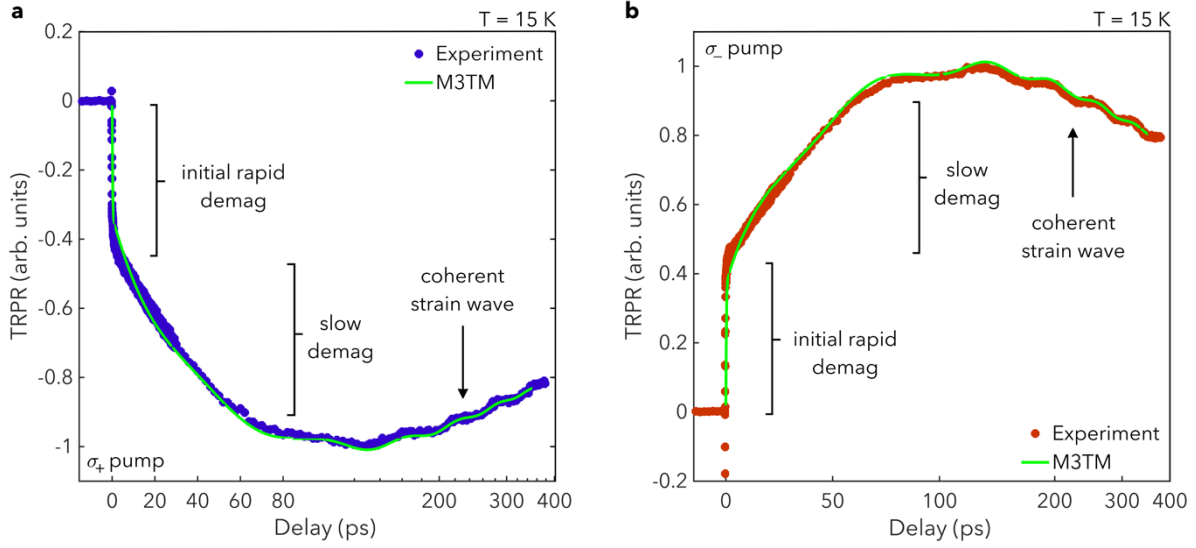
**Supplementary Figure 1. Time-resolved polarization rotation signals and M3TM fits.** Time-resolved polarization rotation signals $T = 15$ K under **a** σ_+ and **b** σ_- pumping. The colored dots are experimental data and the green traces are fits using the M3TM plus a decaying 16 GHz sinusoidal signal obtained by fitting the experimental data.

99   variable-order solver based on the numerical differentiation formulas of orders 1 to 5 for time

100   integration. The resulting M3TM fits for the σ_+ and σ_- pumping conditions are indicated by the

101   green lines in Supplementary Fig. 1 and are calculated as

102
$$TRPR \propto \int m(t,z)e^{-z/\delta_{\mathrm{p}}}dz, \qquad (11)$$

103   where δ_{p} is the penetration depth. The fits in Supplementary Fig. 1 were obtained using fit

104   values of $a_{\mathrm{sf}} = 0.175$, $G_{ep} = 4.05 \times 10^{16}$ J/m³sK, $P_0 = 1.25 \times 10^{-5}$ J/m⁴s, and $\tau_{\mathrm{th}} = 4$ ps for the σ_+
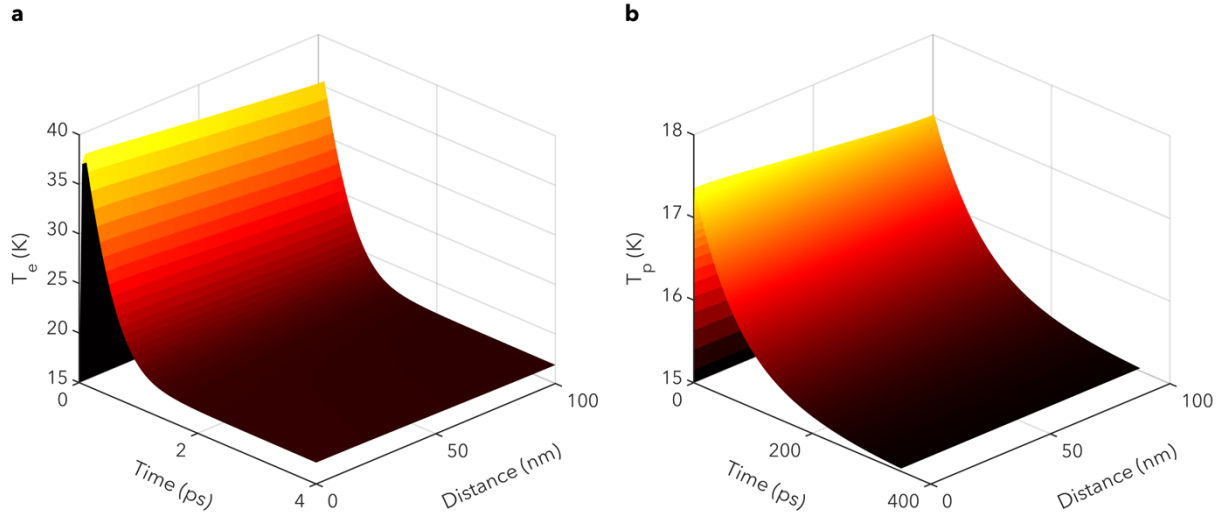
Supplementary Figure 2. Electron and phonon temperatures. a T_e and **b** T_p as a function of time and depth into the sample calculated using the M3TM under σ_+ pumping at $T = 15$ K.
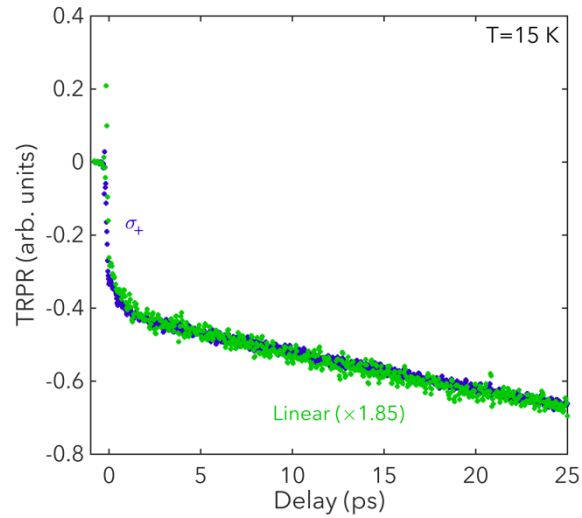
Supplementary Figure 3. Demagnetization dynamics under linear and circular pumping. Demagnetization dynamics in the first 25 ps under σ_+ (blue) and linearly (green) polarized pumping at $T = 15$ K. The linearly polarized data has been normalized by a factor of 1.85 to enable qualitative comparison with the circularly polarized data.
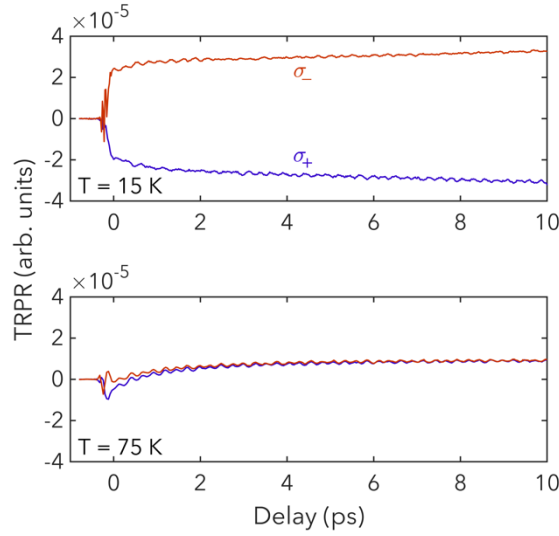
Supplementary Figure 4. Raw TRPR signals under σ_+ and σ_- pumping above and below T_c. Raw TRPR signals under σ_+ (blue) and σ_- (red) pumping below ($T = 15$ K, upper panel) and above ($T = 75$ K, lower panel) T_c.

105   pumping case and $a_{sf} = 0.199$, $G_{ep} = 3.40 \times 10^{16}$ J/m^{3}sK, $P_0 = 1.28 \times 10^{-5}$ J/m^{4}s, and $\tau_{th} =$

106   4.88 ps for the σ_- pumping case. The additional oscillatory component in the M3TM fits,

107   associated with the 16 GHz coherent strain wave, were added by using a decaying sinusoidal fit

108   of the oscillatory components in the experimental data.

109   In addition, Supplementary Fig. 2 shows that the pump pulse causes a transient increase

110   of ~22 K in T_e from the equilibrium temperature of $T_0 = 15$ K that decays back to equilibrium

111   within the first 2 ps. In contrast, the change in the lattice temperature, T_p, upon photoexcitation is

112   only ~2 K and takes several hundred picoseconds to recover back to equilibrium. Finally, we

113   note that while we did not collect long time scale data under the linearly polarized pumping case,

114   we note that the dynamics over the first ~25 ps are nearly identical to the σ_+ dynamics, as shown

115   in Supplementary Fig. 3. Here, we have normalized the linearly polarized data to enable

116   qualitative comparison of the two curves (i.e., the timescales on which relaxation occurs).

117   Accordingly, we do not expect linearly polarized pumping to yield substantively different fitting

118   results.

119

120   *Oscillatory Mode Fitting*

121   We chose to focus on Fourier transform-based analysis of the oscillatory modes, which allowed

122   us to directly extract the helicity-dependent ratio of A_{1g}^1 and A_{1g}^2 modes from the spectral weight

123   in the vicinity of these modes with minimal data processing. This primarily involved removing

124   the non-oscillatory background signals originating from ultrafast demagnetization below T_c or

125   optical effects (e.g., induced birefringence), examples of which are shown in Supplementary Fig.

126   4 for data taken at $T = 15$ K and 75 K. We also performed fitting-based analysis of the time

127   domain waveforms using models consisting of the sums of two exponentially decaying

128   sinusoidal oscillators, each of the form $A_i e^{-t/\tau_i} \sin(\omega_i t + \phi_i)$. Here, the oscillatory component

129   of the experimental signals was first bandpass filtered between 0.5 – 12 THz to remove low and

130   high frequency noise far away from the optical phonon frequency range, which improved the fit

131   quality. The results of the fitting for σ_+ and σ_- pumping at 15 K are shown in the upper panel of

132   Supplementary Fig. 5a, yielding fit frequencies of approximately 2.4 THz and 3.86 THz that

133   correspond to the A_{1g}^1 and A_{1g}^2 modes, respectively, in good agreement with the Fourier

134   transform peak positions. We find that while the fit produces satisfactory results at later times,

135   we observe a deviation from our experimental data in the first ~ 3 ps, indicated by the red shaded

136   regions in Supplementary Fig. 5. We postulate that this is due to the presence of a weak signal

137   associated with a Raman allowed phonons previously associated with AFM ordering[13,14] due to

138   the coexistence of monoclinic and rhombohedral structural phases throughout the volume of the

139　bulk crystal, which was recently confirmed via temperature-dependent X-ray diffraction

140　measurements[15]. To corroborate this, we fit our data
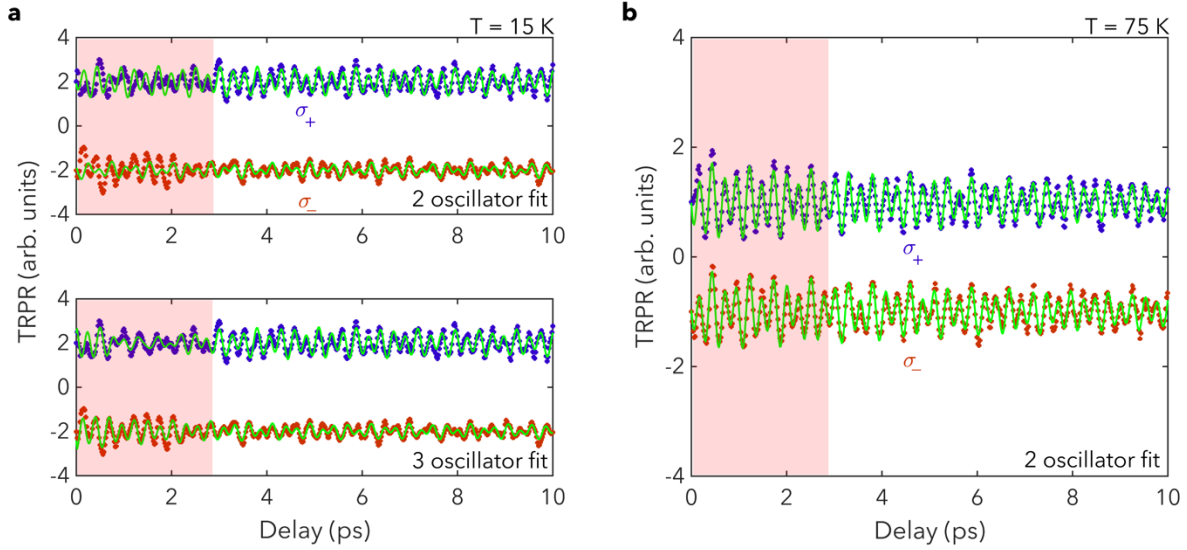
Supplementary Figure 5. Oscillator fitting under σ_+ and σ_- pumping above and below T_C.

a Two-oscillator (upper panel) and three-oscillator (lower panel) fits (green traces) of the bandpass filtered oscillatory component of the measured TRPR signal at $T = 15$ K under σ_+ (blue dots) and σ_- (red dots) pumping and **b** two-oscillator fit (green traces) of the bandpass filtered oscillatory component of the measured TRPR signal at $T = 75$ K under σ_+ (blue dots) and σ_- (red dots) pumping. The red shaded region indicates the temporal window over which the two-oscillator model deviates from the $T = 15$ K experimental data.

141　with a three-oscillator model; the results for σ_+ and σ_- pumping at 15 K are shown in the lower

142　panel of Supplementary Fig. 5a. The fit frequencies of the A_{1g}^1 and A_{1g}^2 modes remain

143　unchanged, and the third mode fit frequency was approximately 3.73 THz. We get improved

144　agreement in the first ~ 3 ps under both pumping configurations. Additionally, the frequency of

145　the third oscillator is in excellent agreement with the AFM order dependent mode frequency

146   measured via spontaneous Raman scattering[13,14]. We also found that this mode rapidly decays

147   (within 2 ps) and the fit amplitude was relatively insensitive to the pump polarization as

148   compared to the A_{1g}^2 mode. In contrast, as shown in Supplementary Fig. 5b, at 75 K (above T_c)

149   we find that the two-oscillator model captures the coherent dynamics over the full temporal

150   window with A_{1g}^1 and A_{1g}^2 mode fit frequencies of approximately 2.4 THz and 3.85 THz,

151   respectively. The lack of a third oscillatory mode above T_c is consistent with the absence of

152   magnetic ordering that would be required to support an AFM order dependent mode. The fits

153   below T_c revealed that the dominant helicity dependence was in the A_{1g}^2 mode, consistent with

154   our Fourier transform analysis. Finally, due to the long decay time of the A_{1g}^1 and A_{1g}^2 modes

155   below T_c, both fitting- and Fourier transform-based approaches were unable to reveal conclusive

156   trends in the decay time of the oscillators across the phase transition.

157

158   *Spin-Wave Spectrum*

159   In our analysis we assumed the spin Hamiltonian

160
$$H_{sp} = \sum_{\langle \mathbf{rr'} \rangle_\gamma} \left[J_{H1} \mathbf{S_r} \cdot \mathbf{S_{r'}} + J_K S_\mathbf{r}^\gamma S_\mathbf{r'}^\gamma \right] + \sum_{\langle\langle \mathbf{rr'} \rangle\rangle} J_{H2} \mathbf{S_r} \cdot \mathbf{S_{r'}} + J_D \, \widehat{\mathbf{D}}_{\mathbf{rr'}} \cdot \mathbf{S_r} \times \mathbf{S_{r'}}$$
$$+ \sum_{\langle\langle\langle \mathbf{rr'} \rangle\rangle\rangle} J_{H3} \mathbf{S_r} \cdot \mathbf{S_{r'}} + \sum_{\langle \mathbf{rr'} \rangle_c} J_{Hc} \mathbf{S_r} \cdot \mathbf{S_{r'}} + \sum_\mathbf{r} J_A \left(S_\mathbf{r}^x + S_\mathbf{r}^y + S_\mathbf{r}^z \right)^2, \qquad (12)$$

161   with exchange constants $(J_{H1}, J_{H2}, J_{H3}, J_K, J_D, J_A, J_{Hc}) = $ (-2.4,-0.1, 0.1, 0.9, -0.2, -0.2, -0.59) meV

162   (more details, including definitions of the exchange constants, etc., are in the main text). The

163   Dzyaloshinskii-Moriya (DM) vector $\widehat{\mathbf{D}}_{\mathbf{rr'}}$ assumes values $\pm \frac{1}{\sqrt{3}}(1,1,1)^T$, with the sign structure in

164   accordance with Ref. 16. The spin Hamiltonian is guided by previous neutron scattering

165   experiments, where it was found that the combination of Heisenberg and DM interactions, along
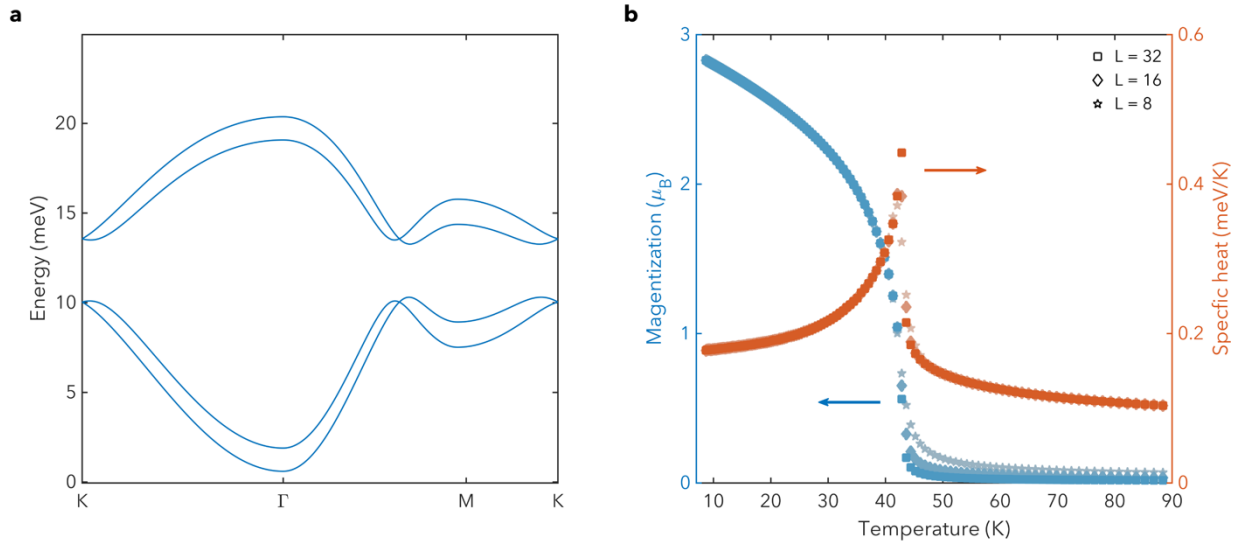
Supplementary Figure 6. Spin-waves and thermodynamics. a The spin-wave spectrum calculated from the equilibrium spin model, equation (12), captures salient features seen in experiments[17]: an overall band width $\sim$20 meV, a zone center excitation gap $\sim$2 meV at the Γ-point, and a gap $\sim$3 meV at the BZ corners (K-points). Note that there are six bands in total, two pairs of which are degenerate. **b** Magnetization and specific heat as determined from MC simulations. The peak in the specific heat indicates the calculated magnetic ordering transition for monolayer CrI_3 at $T_c = 42.8$ K. Opaque curves were obtained at a system size $L = 32$; lighter colors indicate system sizes $L = 8$ and 16 (from lighter to darker). Statistical error bars are smaller than the plot markers.

166   with a local spin anisotropy, yields an excellent fit for the magnon spectrum[18]. However, the fit

167   is not unique. It is possible to introduce finite Kitaev interactions without inducing a significant

168   change in the magnon spectrum: on the level of nearest neighbor interactions, keeping the overall
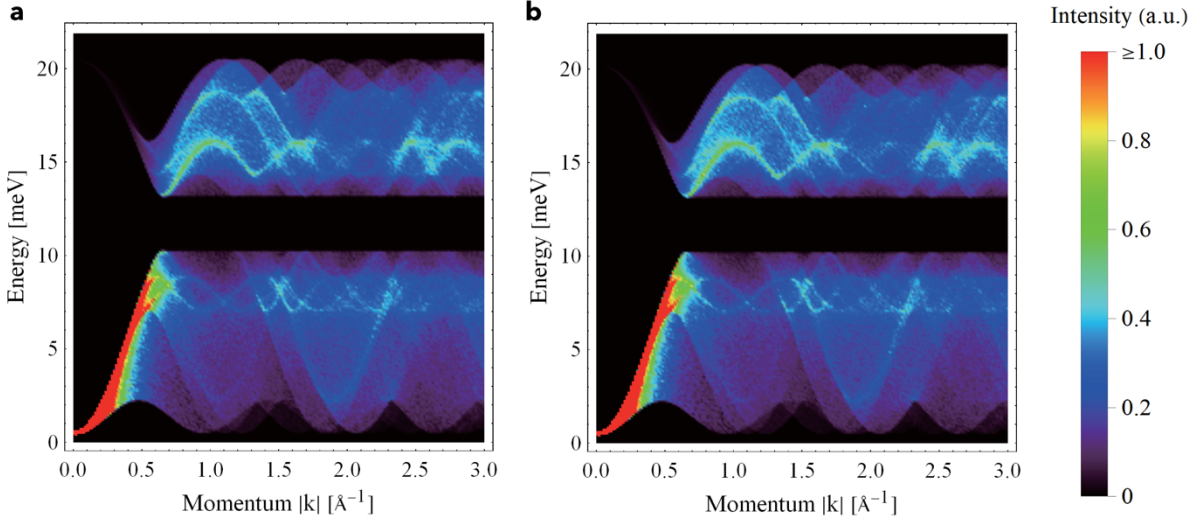
Supplementary Figure 7. Powder diffraction spectrum. a Powder diffraction spectrum for the model parameters, as determined in Ref. 18 in the absence of Kitaev exchange, and **b** model parameters used in this work with a finite Kitaev interaction. Both models provide excellent agreement with the experimentally observed magnon spectrum[18].

169 mean-field energy scale $J_{H1} + K/3$ constant, there is freedom to vary the ratio of Heisenberg and

170 Kitaev contributions. In order to determine the precise ratio of Kitaev and Heisenberg

171 interactions, we draw on previous *ab initio* calculations, which have identified the dominant role

172 of FM Heisenberg interactions ($J_{H1} = -2.4$ meV) augmented by AFM Kitaev couplings ($K = $

173 0.9 meV)[19]. Remarkably, the *ab initio* study also predicted the same nearest-neighbor mean-field

174 energy scale as the neutron scattering experiments, allowing for the two perspectives to be

175 combined easily. The same qualitative structure of FM Heisenberg interactions in conjunction

176 with AFM Kitaev exchange has recently also been identified in strong-coupling perturbation

177 theory[20].

178   As we show in Supplementary Fig. 6a, spin-wave theory calculations for this model

179   reproduce important features of the magnon spectrum; the spin-wave calculations are performed

180   with a six-site unit cell (as defined in Ref. [18]), leading to a six-band spectrum. The key features

181   include a gap at the Brillouin zone (BZ) center which is set by J_A[18], as well as the gap at the

182   Brillouin zone corners which is set predominantly by J_D, with additional minor contributions

183   from J_K[18]. Despite introducing finite Kitaev exchange in our model, as guided by *ab initio*

184   theory, the overall prediction for the intensity distribution in neutron powder diffraction is in

185   excellent agreement with the data obtained in Ref. [18] (see Supplementary Fig. 7).

186   Finally, we mention that a biquadratic spin exchange $(\mathbf{S_r} \cdot \mathbf{S_{r'}})^2$ has also been proposed

187   to be a potentially relevant term in the microscopic description of CrI_3[21]. In our combined spin-

188   phonon model, such terms would automatically emerge upon integrating out the local phonon

189   modes, which couple to the Heisenberg spin exchange of the form $\mathbf{S_r} \cdot \mathbf{S_{r'}}$. Schematically, the

190   terms are obtained when in a Hamiltonian of the form $H = M\Omega X^2/2 + J\Phi X S_i S_j$, where X is the

191   phonon mode and S_i and S_j are spin operators, the phonon mode is integrated out as

192
$$\int DX \, e^{-H} = \int DX \, e^{-\frac{M\Omega}{2}X^2 + J\Phi X S_i S_j} \sim e^{\frac{(J\Phi S_i S_j)^2}{2M\Omega}}, \tag{13}$$

193   However, those terms would scale as $J_{H1}^2\phi^2/M\Omega^2 \approx 10^{-3}$ meV and are therefore negligibly small

194   within our model.

195

196   *Thermodynamics: Monte Carlo Simulations*

197   We carried out classical Monte Carlo (MC) simulations on the spin-phonon system, on

198   layered honeycomb lattices of $2 \times L \times L \times L_c$ spins, with in-plane system sizes up to $L = 32$, the

199   number of layers $L_c = 8$, and periodic boundary conditions. Supplementary Fig. 6b shows the

200   specific heat and magnetization data from our MC simulation results for system sizes $L = 8,16,$

201   and 32 which exhibits an FM phase transition at $T_c = 42.8$ K. It is important to note that our MC

202   simulations are purely classical, whereas the physical $S = 3/2$ spins may still be subject to

203   quantum effects and a partial rescaling towards the quantum spin exchange energy scale $S(S +$

204    $1)$, exceeding the classical energy scale S^2 and bringing T_c closer to the experimental value.

205   This has previously been noted for CrI$_3$ in Ref. [22] and incorporating such quantum corrections by

206   rescaling to the effective spin length $S_{\text{eff}} = \sqrt{S(S+1)}$, with $S = 3/2$ for Cr shifts T_c up from its

207   classical value by a factor of 5/3. Our classical MC simulations thus yield an enhanced

208    $T_c(3D)\sim71$ K, which compares favorably with the experimental bulk T_c of ~61 K. Quantum

209   rescaling similarly manifests in other systems, for example for the $S = 1/2$ Heisenberg model on

210   the cubic lattice, where T_c/J is found to be 0.95 in quantum Monte Carlo calculations[23], whereas

211   the classical value is $T_c/J = 1.44/4 \approx 0.36$; this amounts to a phenomenological rescaling of 2.9,

212   close to the value of $S(S+1)/S^2 = 3$ [24].

213

214   *Phonon Coupling and Spin-Phonon Dynamics*

215   As described in the main text, we incorporate spin-phonon coupling to the dominant

216   Heisenberg exchange constant by $\tilde{J}_{H1,\mathbf{rr'}} = J_{H1}\left(1 + \frac{\phi}{2}(X_{\mathbf{r}} + X_{\mathbf{r'}})\right)$, with spin-phonon coupling

217   parameter ϕ. The spin-phonon coupling may be constrained using our DFT calculations. From

218   the model Hamiltonian, we find that the energy difference per spin between the (in-plane) AFM

219   and FM states is given by $\Delta E = S^2(3\tilde{J}_{H1} + J_K + 3J_{H3})$, where $\tilde{J}_{H1}$ is the mean value of $\tilde{J}_{H1,\mathbf{rr'}}$

220   across all lattice bonds. Assuming a uniform phonon displacement X, we find $\partial\Delta E/\partial X =$

221    $S^2(3J_{H1}\phi)$. Choosing $\phi = 1.98$ Å^{-1} we obtain $\partial\Delta E/\partial X = -32$ meV/Å, in agreement with our

222   DFT estimate. For simplicity, as $J_{H2}, J_{H3}, J_K, J_D, J_A$, and J_{Hc} are already small compared to the

223   nearest-neighbor Heisenberg exchange J_{H1}, we neglect phonon coupling to these exchange

224   constants since it is not expected to have a significant impact on our results.

225   The impact of the pump pulse can be simulated as a sudden change in the local lattice

226   displacement $X_{\mathbf{r}}$ by a combination of a magnetization-independent term and a term which is

227   linear in the magnetization m. This is parametrized by two numbers, ξ_1 and ξ_2, according to

$$X_{\mathbf{r}} \rightarrow X'_{\mathbf{r},\sigma} = X_{\mathbf{r}} + \xi_1(1 + \sigma\xi_2 m_{\mathbf{r}}). \tag{13}$$

229   In our simulations, we chose $\xi_1 = 0.01$ Å; as discussed further below, however, its value does

230   not impact the ratio of Fourier components $m_+(\Omega)/m_-(\Omega)$. Further, we found that $\xi_2 \approx 0.18/\mu_B$

231   led to good agreement with the experimental observation of the pump-helicity dependent

232   asymmetry. In this supplemental section, we provide additional rationales for the functional form

233   of the lattice distortion and its properties.

234   Assuming thermal equilibrium, the mean phonon displacement X can be determined by

235   minimizing the coupled spin-phonon Hamiltonian $H = H_{\text{ph}} + H_{\text{sp}}$ with respect to X, i.e, setting

236    $\partial H/\partial X = 0$. This leads to

$$M\Omega^2 X = -\sum_{\langle \mathbf{rr'}\rangle} J_{H1}\phi\mathbf{S}_{\mathbf{r}} \cdot \mathbf{S}_{\mathbf{r'}}. \tag{14}$$

238   In the magnetically ordered phase, using a mean-field picture with average magnetization $\langle S_{\mathbf{r}}\rangle =$
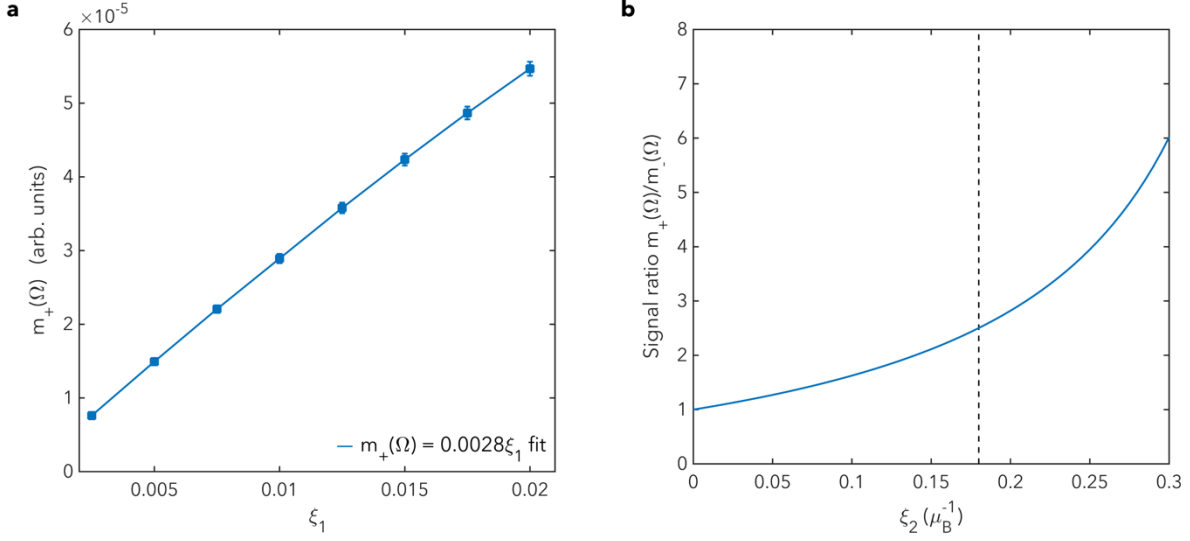
Supplementary Figure 8. Dynamical simulation parameters. a Response of the Fourier component $m_+(\Omega)$ at the phonon frequency Ω as a function of ξ_1 of the phonon (for the case $\xi_2 = 0$). Data is displayed at $T/T_c = 0.6$. It is fit by a linear function $m_+(\Omega) = 0.0028\xi_1$. **b** The Fourier component ratio $m_+(\Omega)/m_-(\Omega)$ as a function of ξ_2, based on the linear fit shown in **a**. The dashed line in **b** indicates $\xi_2 \approx 0.18/\mu_B$, as determined in the main text.

239   $m/(2\mu_B)$, we thus naturally find that the equilibrium phonon displacement scales quadratically

240   with the magnetization,

241
$$\langle X \rangle \approx \alpha m^2, \tag{15}$$

242   with $\alpha = -3J_{H1}\phi/(8M\Omega^2\mu_B^2)$. This is consistent with the magnetostriction respecting time-

243   reversal symmetry, i.e., it is invariant under $m \to -m$. At a temperature of $T/T_c = 0.6$, for

244   example, our MC simulations indicate $\langle m \rangle \approx 2.4\mu_B$ (i.e., $\langle S_r \rangle = 1.2$) and $\langle X \rangle \approx 4.9 \times 10^{-4}$ Å,

245   yielding a proportionality constant of $\alpha \approx 8.5 \times 10^{-5}$ Å$/\mu_B^2$. This value compares well with the

17

246   mean-field picture, which, neglecting local fluctuations in the magnetization, predicts $\alpha = $

247   7.5×10^{-5} Å$/\mu_B^2$.

248   Given that the pump pulse is an intense non-equilibrium drive, for which we do not have

249   a detailed microscopic model, we discuss phenomenological pictures for the pump-induced

250   dynamics. The pump pulse can, through helicity-dependent perturbations in the local Cr moment,

251   induce a change in magnetization by $\pm\delta$, depending on the photon polarization $\sigma = \pm 1$. This

252   change in magnetization can impact the phonon coordinate via the relation in equation (15),

253   leading to an additional lattice distortion component expressed as

$$\langle X'_\sigma \rangle = \alpha(m + \sigma\delta)^2 = \langle X \rangle + \alpha\delta^2 + 2\sigma\alpha m\delta, \tag{16}$$

255   which is of the form used in equation (13) with $\xi_1 = \alpha\delta^2$ and $\xi_2 = 2/\delta$. Such a process leads to

256   a one-parameter description of the lattice distortion, controlled by δ.

257   Whereas the choice of parameters ξ_1 and ξ_2 fulfills the relation $\xi_1 = 4\alpha/\xi_2^2$ from the

258   single-parameter description with the proportionality constant α as determined above, the

259   magnetization change δ implied by the value of $\xi_2 \approx 0.18/\mu_B$ would be unphysically large. The

260   one-parameter picture thus cannot be complete. An important alternative mechanism for

261   explaining our results is based on Raman transitions induced by the incident photons via virtual

262   intermediate state excitations from the iodine $5p$ to chromium e_g states. The intermediate singly

263   occupied e_g level is Jahn-Teller active, which can lead to an additional trigonal lattice distortion

264   in the Raman process. The e_g level is expected to be spin-split in the presence of magnetic order,

265   and the photon polarization determines the spin of the virtually excited electron, which can be

266   accounted for by a displacement $W_1 + \sigma m W_2$ (which is again invariant under simultaneous

267   inversion of the sign of the magnetization and the incoming photon polarization). If this effect

268   dominates, the phonon coordinate would be modified as $\langle X'_\sigma \rangle = \langle X \rangle + W_1 + \sigma m W_2$, so that $\xi_1 =$

269   W_1 and $\xi_2 = W_2/W_1$. In effect, ξ_1 controls the overall lattice distortion strength and the resulting

270   coherent oscillation amplitude (averaged over pump photon helicity), while ξ_2 controls the

271   pump-helicity dependent asymmetry in the coherent dynamics.

272   　　　　Modeling the lattice distortion in the manner described above robustly leads to the ratio

273   of Fourier components $m_+(\Omega)/m_-(\Omega)$ shown in Fig. 3c of the main text. To corroborate this, we

274   make the plot shown in Supplementary Fig. 8a, which shows that the response $m_+(\Omega)$ to an

275   impulsive perturbation of the phonon displacement is approximately proportional to the

276   magnitude of the strength ξ_1 (neglecting any splitting ξ_2 for simplicity).

277   　　　　The non-equilibrium pump-induced lattice displacement naturally affects the signal-to-

278   noise ratio in our model calculations, such that a weaker kick is more difficult to detect unless we

279   average over a larger number of ensemble configurations. Due to the linear scaling, the ratio of

280   Fourier components $m_+(\Omega)/m_-(\Omega)$ is independent of ξ_1; its dependence on ξ_2 is shown in

281   Supplementary Fig. 8b. Furthermore, the helicity-dependent asymmetry linearly depends on the

282   magnetization. Consequently, the functional form of the ratio of Fourier components should have

283   a similar characteristic onset as the magnetization curve below T_c, which we indeed observe, c.f.

284   the magnetization curve in Supplementary Fig. 6b.

285
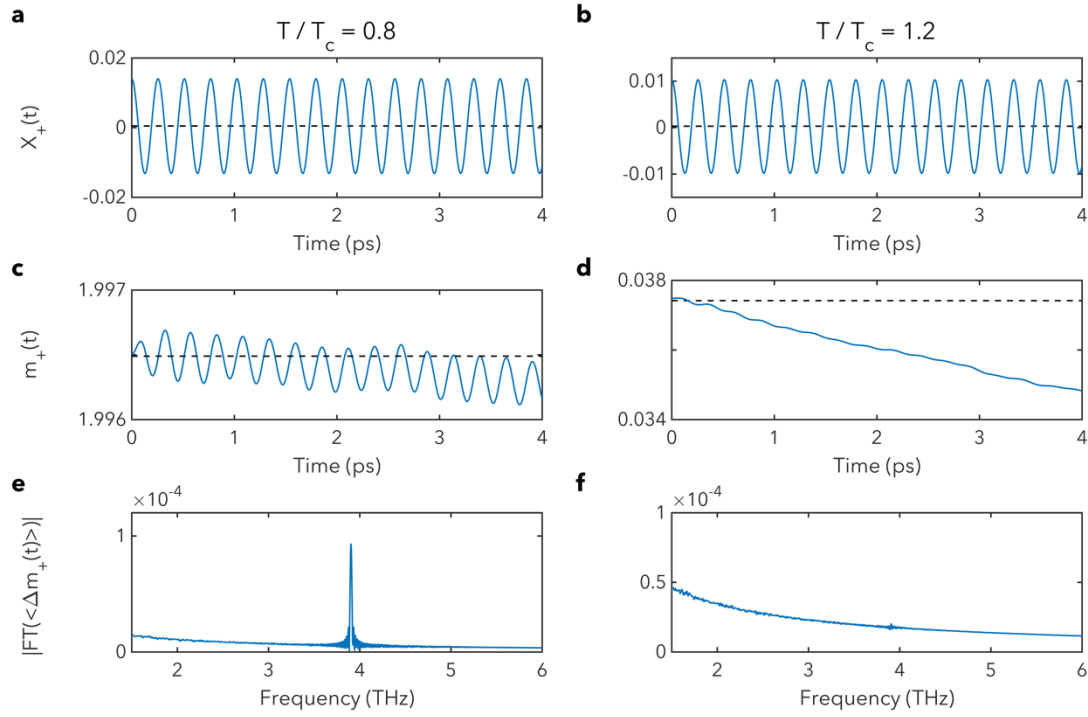
Supplementary Figure 9. Simulations of the vibrational and magnetization dynamics.
Simulation results showing phonon coordinate coherent oscillations in both **a** the magnetically
ordered phase at $T < T_c$ and **b** the paramagnetic regime for $T > T_c$. The dashed lines represent
the thermodynamic equilibrium value. The magnetization shows coherent oscillations **c** in the
FM phase below T_c, but not **d** in the paramagnetic phase above T_c. The Fourier transformation
of the magnetization shows a pronounced peak at the phonon frequency **e** in the FM phase below
T_c, but not **f** in the paramagnetic phase above T_c. All data shown assumes σ_+ polarized light.

286   *Pump-Induced Dynamics: Coherent Oscillations*

287   Here, we show two examples of datasets for the time evolution of the coupled spin-

288   phonon model Hamiltonian. After application of the initial shift in lattice displacement, the

289   phonon oscillates coherently, regardless of whether the system is in the magnetically ordered

290   phase or in the paramagnetic phase; see Supplementary Fig. 9a and Supplementary Fig. 9b,

291   respectively. Qualitatively different behavior, however, is observed in the time dependence of

292   the magnetization. While in the FM phase the coherent phonon oscillations effectively couple to

293   the magnetization, yielding coherent magnetization oscillations (Supplementary Fig. 9c), such

294   coupling is not observed above T_c. In the latter case the magnetization merely shows a

295   demagnetizing drift, as expected after heating the system; short-time oscillations at the phonon

296   frequency are not observed (Supplementary Fig. 9d) (note that the finite magnetization in the

297   paramagnetic phase is an artifact of the finite system size, as also seen in Supplementary Fig.

298   6b). Consequently, a sharp phonon-induced signal in the Fourier spectrum of the magnetization

299   is only visible below T_c (Supplementary Fig. 9e and Supplementary Fig. 9f).

300

301   *Comparison of Different Models for the Spin-Phonon Dynamics*

302   In the main manuscript we have employed a spin model based on the layered honeycomb model,

303   in which the magnetic moments couple to local phonon modes at every lattice site. The model is

304   chosen to closely resemble the bulk CrI_3 flakes that were used in the experiment. However, as we

305   shall demonstrate below, the same phenomenology can also be observed for a simplified model

306   of a single honeycomb layer, or even when the local phonon modes are replaced by a single

307   global mode.

308   The full model is governed by the microscopic Hamiltonian $H = H_{\mathrm{ph}} + H_{\mathrm{sp}}$, with the

309   phonon and spin contributions as specified in the main manuscript and parametrized by the spin

310   exchange constants $(J_{H1}, J_{H2}, J_{H3}, J_K, J_D, J_A, J_{Hc})$. We refer to this model as the 3D model with

311   local phonons. We now define a simplified single-layer model, i.e., we set the interlayer coupling

312    $J_{Hc} = 0$ and refer to this as the 2D model with local phonons. When performing numerical
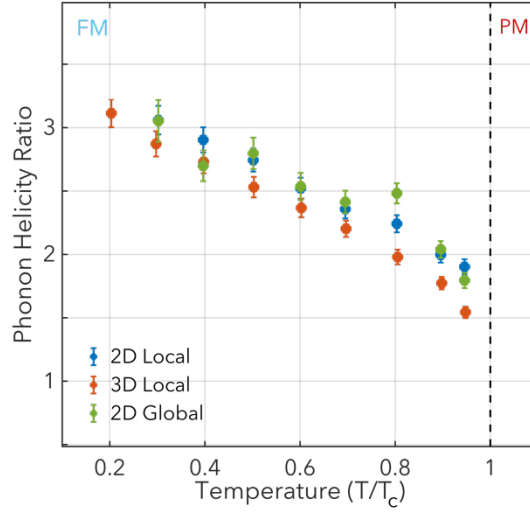
Supplementary Figure 10. Comparison of different models for spin-phonon dynamic simulations. The σ_+/σ_--ratio of integrated Fourier transform peaks at the A_{1g}^2 mode frequency is shown for three different models: a three-dimensional model for bulk CrI_3 with local phonon modes (red) and a two-dimensional model for single layer CrI_3 with either local phonon modes (blue) or global phonon modes (green).

313   simulations, it is thus sufficient to consider a single honeycomb layer of $2 \times L \times L$ spins. From the

314   2D model with local phonons we further derive the 2D model with a single phonon

315   mode by enforcing $X_{\mathbf{r}} = X_{\mathbf{r}'} \equiv X$ and $P_{\mathbf{r}} = P_{\mathbf{r}'} \equiv P$ for all lattice sites $\mathbf{r}$ and $\mathbf{r}'$, such that the

316   model only has one effective global phonon mode. In the dynamic simulation, the pump pulse is

317   then modeled as a change in the global phonon displacement X, which depends on the global

318   average magnetization m, in analogy to the modeling that was used for local displacement $X_{\mathbf{r}}$

319   and local magnetization $m_{\mathbf{r}}$.
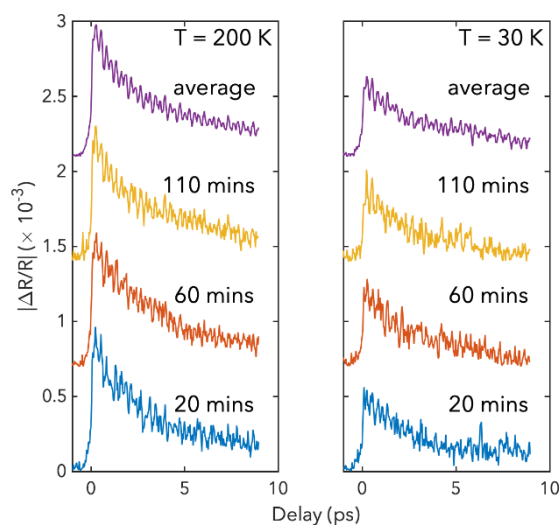
Supplementary Fig. 11. Long-time stability of the time-resolved differential reflectivity.
Individual (i.e., not averaged) differential reflectivity traces taken at 20 minutes (blue), 60
minutes (red), and 110 minutes (yellow), as well as averages over 10 scans taken over the full
110 minutes measurement timeframe (purple) at 200 K and 30 K at a pump fluence of
0.64 mJ/cm^2.
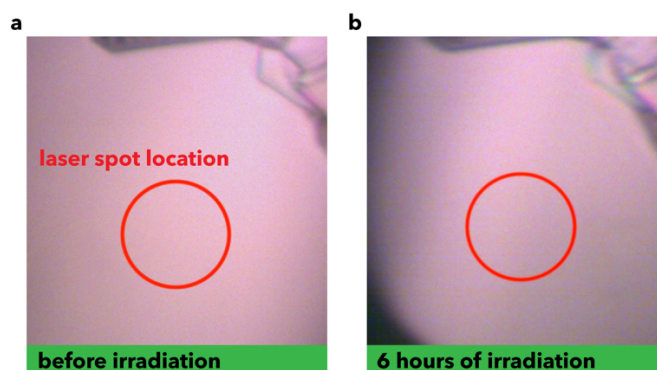
Supplementary Fig. 12. Sample quality before and after irradiation. Sample images
taken using a 20X objective (a) before and (b) after 6 hours of continuous irradiation at 1.55
eV and a fluence of 0.64 mJ/cm^2. The location of the laser spot is denoted by the red circle.

320   The phonon helicity ratio plotted in Supplementary Fig. 10 shows no significant

321   difference between the three different models. The small deviation that is discernible between the

322   data for the 3D model and the data for the 2D models can be attributed to the slightly different

323   onset of the magnetization curves for $T < T_c$.

324

325   *Sample Quality Under Laser Irradiation*

326   To confirm that the sample quality remained constant throughout the lifetime of the experiment

327   at the 0.64 mJ/cm^2 pump laser fluence used in our experiments, we conducted time- resolved

328   differential reflectivity measurements in a crossed polarized configuration above and below T_c.

329   Supplementary Fig. 11 shows the results for the two cases. The left-hand panel shows individual

330   (i.e., not averaged) time-resolved differential reflectivity scans taken at $T = 200$ K after 20

331   minutes (blue), 60 minutes (red), and 110 minutes (yellow) of continuous irradiation. No

332   appreciable change in the traces is observed on these long timescales, and the signals are

333   consistent with the average over 10 scans taken over the full 110 minutes experimental runtime

334   shown in purple. We see no significant difference in the amplitude or decay rate of the coherent

335   oscillations, nor in the overall exponential decay dynamics attributable to electron-phonon

336   coupling. The same is true for the data taken at $T = 30$ K, as shown in the right-hand panel of

337   Supplementary Fig. 11. Here, we see consistent results for scans taken at the three elapsed

338   experimental times that are again mutually consistent with the 10-scan average. Finally, to

339   further confirm that no sample degradation took place at our defined fluence, Supplementary Fig.

340   12 shows microscope images captured before and after 6 hours of continuous laser irradiation at

341   0.64 mJ/cm^2. Here the red circles indicate the location of the pump and probe focal spots,

342   revealing no discernible darkening or other marring of the surface; these results clearly
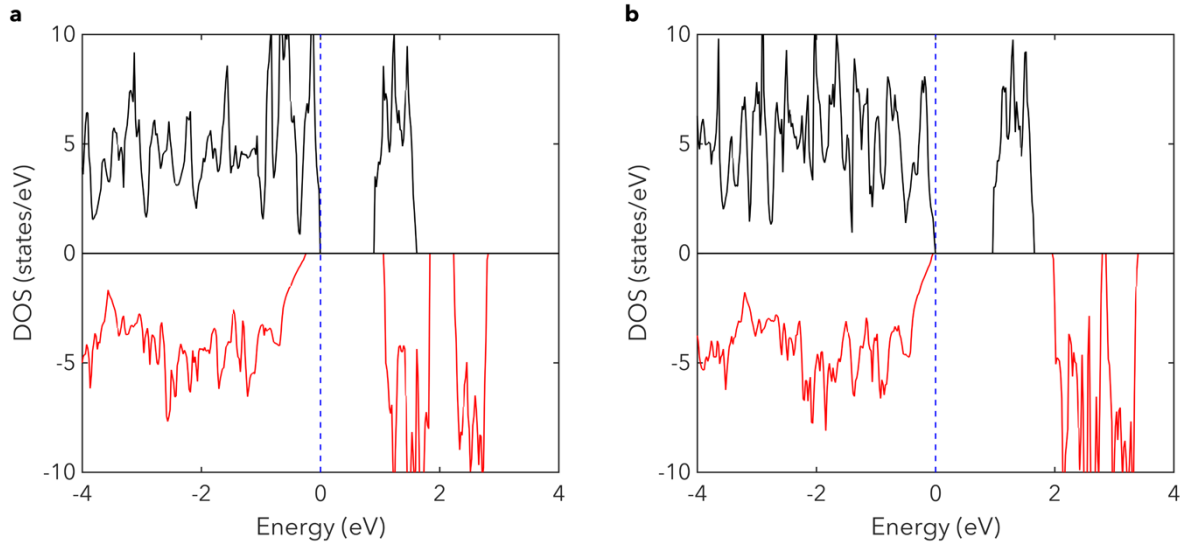
Supplementary Figure 13. Density of states for bulk CrI₃. Density of states (DOS) for bulk CrI$_3$ calculated with **a** LDA and **b** LDA+U. The spin-up component (black) has positive values, and the spin-down component (red) has negative values. The value of the Hubbard interaction on the Cr-$3d$ orbitals is $U = 2.2$ eV.

343   demonstrate that the sample properties did not significantly change over the data acquisition

344   time.

345

346   **References**

347   1.   Wu, M., Li, Z., Cao, T. & Louie, S. G. Physical origin of giant excitonic and magneto-

348   optical responses in two-dimensional ferromagnetic insulators. *Nat. Commun.* **10**, 2371

349   (2019).

350   2.   Seyler, K. L. Probing valley and magnetic photoexcitations in 2D crystals and their

351   heterostructures. (University of Washington, 2018).

352   3.   Ščajev, P., Gudelis, V., Jarašiūnas, K. & Klein, P. B. Fast and slow carrier recombination

353   transients in highly excited 4H– and 3C–SiC crystals at room temperature. *J. Appl. Phys.*

354   **108**, 023705 (2010).

355   4.   Carva, K., Battiato, M. & Oppeneer, P. M. Ab initio investigation of the Elliott-Yafet

356   electron-phonon mechanism in laser-induced ultrafast demagnetization. *Phys. Rev. Lett.*

357   **107**, 207201 (2011).

358   5.   Park, J., Zhou, J.-J. & Bernardi, M. Spin-phonon relaxation times in centrosymmetric

359   materials from first principles. *Phys. Rev. B* **101**, 045202 (2020).

360   6.   Koopmans, B. *et al.* Explaining the paradoxical diversity of ultrafast laser-induced

361   demagnetization. *Nat. Mater.* **9**, 259–265 (2010).

362   7.   Sheng, H., Zhu, Y., Bai, D., Wu, X. & Wang, J. Thermoelectric properties of two-

363   dimensional magnet CrI_3. *Nanotechnology* **31**, 315713 (2020).

364   8.   McGuire, M. A., Dixit, H., Cooper, V. R. & Sales, B. C. Coupling of crystal structure and

365   magnetism in the layered, ferromagnetic insulator CrI_3. *Chem. Mater.* **27**, 612–620 (2015).

366   9.   Perry, D. L. *Handbook of Inorganic Compounds*. (CRC Press, 2011).

367   10.   Lin, G. T. *et al.* Critical behavior of two-dimensional intrinsically ferromagnetic

368   semiconductor CrI_3. *Appl. Phys. Lett.* **112**, 072405 (2018).

369   11.   Liu, Y. & Petrovic, C. Three-dimensional magnetic critical behavior in CrI_3. *Phys. Rev. B*

370   **97**, 014420 (2018).

371   12.   Byrd, R. H., Gilbert, J. C. & Nocedal, J. A trust region method based on interior point

372   techniques for nonlinear programming. *Math. Program.* **89**, 149–185 (2000).

373   13.   McCreary, A. *et al.* Distinct magneto-Raman signatures of spin-flip phase transitions in

374   CrI$_3$. *Nat. Commun.* **11**, 3879 (2020).

375   14.   Jin, W. *et al.* Tunable layered-magnetism–assisted magneto-Raman effect in a two-

376   dimensional magnet CrI$_3$. *Proc. Natl. Acad. Sci.* **117**, 24664–24669 (2020).

377   15.   Meseguer-Sánchez, J. *et al.* Coexistence of structural and magnetic phases in van der

378   Waals magnet CrI$_3$. *Nat. Commun.* **12**, 6265 (2021).

379   16.   Chen, L. *et al.* Topological spin excitations in honeycomb ferromagnet CrI$_3$. *Phys. Rev. X*

380   **8**, 041028 (2018).

381   17.   Lee, I. *et al.* Fundamental spin interactions underlying the magnetic anisotropy in the

382   Kitaev ferromagnet CrI$_3$. *Phys. Rev. Lett.* **124**, 17201 (2020).

383   18.   Chen, L. *et al.* Magnetic anisotropy in ferromagnetic CrI$_3$. *Phys. Rev. B* **101**, 134418

384   (2020).

385   19.   Xu, C., Feng, J., Xiang, H. & Bellaiche, L. Interplay between Kitaev interaction and single

386   ion anisotropy in ferromagnetic CrI$_3$ and CrGeTe$_3$ monolayers. *npj Comput. Mater.* **4**, 57

387   (2018).

388   20.   Stavropoulos, P. P. & Kee, H.-Y. Magnetic anisotropy in spin-3/2 with heavy ligand in

389   honeycomb Mott insulators: application to CrI$_3$. *arXiv:2009.04475* 1–12 (2020).

390   21.   Wahab, D. A. *et al.* Quantum Rescaling, Domain Metastability, and Hybrid Domain-

391   Walls in 2D CrI$_3$ Magnets. *Adv. Mater.* **33**, 2004138 (2021).

392   22.   Liu, L., Lin, Z., Hu, J. & Zhang, X. Full quantum search for high T$_c$ two-dimensional van

393   der Waals ferromagnetic semiconductors. *Nanoscale* **13**, 8137–8145 (2021).

394   23.   Sandvik, A. W. Critical Temperature and the Transition from Quantum to Classical Order

395   Parameter Fluctuations in the Three-Dimensional Heisenberg Antiferromagnet. *Phys. Rev.*

396   *Lett.* **80**, 5196–5199 (1998).

397   24.   Peczak, P., Ferrenberg, A. M. & Landau, D. P. High-accuracy Monte Carlo study of the

398   three-dimensional classical Heisenberg ferromagnet. *Phys. Rev. B* **43**, 6087–6093 (1991).

399